Magnetic Rotating Flow of a Hybrid Nano-Materials Ag-MoS$_2$ and Go-MoS$_2$ in C$_2$H$_6$O$_2$-H$_2$O Hybrid Base Fluid over an Extending Surface Involving Activation Energy: FE Simulation

Bagh Ali [1,†] ![ORCID], **Rizwan Ali Naqvi** [2,†] ![ORCID], **Dildar Hussain** [3] ![ORCID], **Omar M. Aldossary** [4,*] ![ORCID] and **Sajjad Hussain** [5,*]

1   School of Science, Department of Applied Mathematics, Northwestern Polytechnical University, 127 West Youyi Road, Xi'an 710072, China; baghalisewag@mail.nwpu.edu.cn
2   Department of Intelligent Mechatronics, Sejong University, Seoul 100083, Korea; rizwanali@sejong.ac.kr
3   School of Computational Sciences, Korea Institute for Advanced Study(KIAS), 85 Hoegiro Dongdaemun-gu, Seoul 02455, Korea; hussain@kias.re.kr
4   Department of Physics and Astronomy, College of Science, King Saud University, P.O. Box 2455, Riyadh 11451, Saudi Arabia
5   School of Aerospace and Mechanical Engineering, Nanyang Technological University, Singapore 639798, Singapore
*   Correspondence: omar@ksu.edu.sa (O.M.A.); sajjadgut@gmail.com (S.H.)
†   Bagh Ali and Rizwan Ali Naqvi are Co-first author, these authors contributed equally to this work.

Abstract: Numeric simulations are performed for a comparative study of magnetohydrodynamic (MHD) rotational flow of hybrid nanofluids (MoS$_2$-Ag/ethylene glycol-water (50–50%) and MoS$_2$-Go/ethylene glycol-water (50–50%)) over a horizontally elongated plane sheet. The principal objective is concerned with the enhancement of thermal transportation. The three-dimensional formulation governing the conservation of mass, momentum, energy, and concentration is transmuted into two-dimensional partial differentiation by employing similarity transforms. The resulting set of equations (PDEs) is then solved by variational finite element procedure coded in Matlab script. An intensive computational run is carried out for suitable ranges of the particular quantities of influence. The primary velocity component decreases monotonically and the magnitude of secondary velocity component diminishes significantly when magnetic parameter, rotational parameter, and unsteadiness parameter are incremented. Both the primary and secondary velocities are smaller in values for the hybrid phase Ag-MoS$_2$ than that of hybrid phase Go-MoS$_2$ but the nanoparticle concentration and temperature are higher for hybrid phase Ag-MoS$_2$. The increased values of parameters for thermophoresis, Brownian motion, shape factor, and volume fraction of ϕ_2 made significant improvement in the temperature of the two phases of nano liquids. Results are also computed for the coefficients of skin friction(x, y-directions), Nusselt number, and Sherwood number. The present findings manifest reasonable comparison to their existing counterparts. Some of the practical engineering applications of the present analysis may be found in high-temperature nanomaterial processing technology, crystal growing, extrusion processes, manufacturing and rolling of polymer sheets, academic research, lubrication processes, and polymer industry.

Keywords: magnetohydrodynamic; hybrid nanofluid; finite element method; shape factor; rotating frame

1. Introduction

Global warming and environmental pollution are ultimately leading to energy shortages in the modern world. As a result, engineers and scientists are looking for new advances in energy for sustainable improvement. Based on current advances in nanotechnology, the improvement of nanomaterials is considered to be more effective in enhancing the thermal efficiency of base liquids. Nanomaterials are mostly used as a coolant in industrial, mechanical, and chemical fields. Liquid cooling is currently a major problem because efficient heat and mass transfer fluids need to provide appropriate conditions for commercial applications. It can be obtained by immersing micro-sized nanomaterials in ordinary base liquids. These fluids are classified as nanofluids and can be commonly used in numerous manufacturing applications such as cooking processing, air condition, automobile radiators, waste heat recovery, refrigeration, etc. Furthermore, Maxwell [1] proposes the innovative idea of adding solid particles to heat transfer fluids to rise their thermal conductivity thermodynamic parameter further discoveries that are put forth by Choi [2] and Kang et al. [3]. They experimented on an empirical model which develop a scope in heat exchange and give researchers a road map to develop new models for hybrid nanoparticles by the matter of fact that its thermal conductivity is more than that of the alone nanoparticle. Another phenomenon that which is discussed here is natural convection which is independent of the motion of fluid over external source such as pump or suction devices, the parameter that is responsible for the motion of the fluid is generally natural fluid or we can pronounce it as buoyancy force. The followings are the practical usage of these parameters. Stagnation point flow of Cu-TiO$_2$/H$_2$O hybrid Nanofluid under the effects of the magnetic field. Ghadikolai et al. [4] described their investigation on heat transfer and shape factors on stretching surfaces. The analysis of convective Poiseuille boundary layer flow of Al$_2$O$_3$/C$_2$H$_6$O$_2$ nanofluid over porous wavy channel has been presented by Zeeshan et al. [5]. Anwar and Rasheed [6] experimented on non-isothermal boundaries in MHD fractional inertial flow with the help of a finite-difference scheme and describe the numerical results on heat transfer. The shape factor and thermal influences on heat transfer and 3D squeezing flow of Ag-Fe$_3$O$_4$/Ethylene.

Dinarvand S et al. [7] investigate the mathematical model name for the Tiwari-Das nanofluid model based on three different water-based nanofluids (copper, alumina, titanium). This examination is interested in developed the homotopy analysis of the stagnation-point flow of MHD mixed convection with electrically conducted permeable vertical stretching/shrinking sheet. Afterward, Mabood et al. [8] provide mathematical research on the properties of MHD stagnation point flow and heat transfer expending the Tiwari-Das nanofluid model. In 2017 the Pop et al. [9] also evaluate the free convective flow of hybrid nanofluid of coper water over the downward-pointing cone through the Tiwari-Das model. Subsequently, after a short cooling down in 2018 Aghamajidi et al. [10] make a similar work on the downward-pointing cone with the effect of rotation and natural convection of hybrid nanofluids. Ghadikolaei et al. [11] performed the Glycol-water nanofluid over the rotating and stretching channel. The outcomes of this research came to discover the reduction of thermal boundary layer thickness. Due to this phenomenon, LTNE porous model has been applied to natural convection of micropolar nanofluid consisting CuO of nanoparticles and H$_2$O base fluid inside a cavity by Izadi et al. [12]. Xu and Xing [13] described the lattice Boltzmann model for nanofluid natural convection in a porous cavity. It was found that nanofluid and porous media causes to intensify natural convection. Shape nanoparticle, joule heating, and thermal radiation impacts on MHD flow of non-Newtonian micropolar dusty fluid by hybrid nanoparticles discussed by Ghadikolaei et al. [14]. The outcomes of the research lead to conclude that the heat transfer rate is efficiently more than alone nanoparticles. The study of natural convection heat transfer of glycol-water inside a cavity has been studied by Solomon et al. [15].

Buongiorno [16] encouraged the important features of the thermophoresis and Brownian motion for the development of heat transfer aspects allied with nanofluids. Bhatti et al. [17] investigate and evaluate the thermos-diffusion properties in Williamson nanofluid overwhelmed in the porous medium by the Buongiorno model. Additionally, Hayat et al. [18] create a dynamic approach

and apply the Buongiorno model on thixotropic nanofluid along with radiation effects and Joule heating. Hassan et al. [19] evaluate the Buongiorno model to improve the thermal conductivity in the Falkner–Skan magnetized nanofluid in the presence of microorganisms. Khan et al. [20] studied the free convection effect on nanofluid flow using vertical plate geometry.

Magnetohydrodynamics (MHD) engagement has valuable implementations in the area of medication, astronomy, advanced plane design, successfully deal with the heat transfer rates in cylinders, numerous machines, energy generators, and turbulent pumps. The MHD effect is discussed as a magnetic effect upon the electric conductor. It relates to the interaction between magnetic fields and electric conductor fluids. Nayak [21] deliberated the thermal radiation effects upon the depth of the molecules and concluded that decreasing the heat transfer is due to thermal radiation and viscous dissipation. Rasheed and Anwar [22] integrated the MHD viscoelastic fluid flow under the effect of homogeneous reaction using partial differential equations. Naz et al. [23] illustrated the effects of MHD flow in a horizontal channel utilizing the Adomian decomposition technique. More work on magnetohydrodynamics theory is carried out [24–27].

In recent years, the investigation of fluid and heat transport problems in the rotating frame is an absolutely charming matter. It is a result of their colossal applications in the assembling of crystal development, computer stockpiling devices, thermal power stations, food handling, diffusive filtration process, rotating machinery, viscometry, and gas turbine rotors [28,29]. The principal endeavor toward this path was made by Wang [30]. The impact of magnetohydrodynamics (MHD) in rotating liquid is studied by Takhar et al. [31]. Nazar et al. [32] examined the unsteady flow in the rotatory frame incited by the deforming sheet. The influence of variable thermal conductivity on 3D Williamson rotating fluid is investigated by Khan et al. [33]. Recently, published research articles on rotating flow are mentioned in [34–37].

This numeric investigation pertains to the two different hybrid nano liquids rotational flow over a plane sheet that stretches horizontally. The novelties of the current study are (i) a comparative study of two hybrid nanofluids with hybrid base fluid and different shape factors, i.e., MoS_2-Ag/ethylene glycol-water (50–50%) and MoS_2-Go/ethylene glycol-water (50–50%), (ii) the Buongiorno nanofluid model is implemented together with Tiwari and Das nanofluid model, (iii) incorporate the chemical reaction and activation energy, and (iv) the finite element approach for this elaborated problem. It solves the boundary value problems adequately, rapidly, and precisely [38,39]. Differentiated outcomes for temperature, Nusselt number, velocity components, skin friction coefficients, nanoparticle volume fraction, and Sherwood number are evaluated and presented. The numerical procedure (FEM) has established reliable results as verified through their comparison with those of existing formerly. Some of the practical engineering utilization of the present investigation might be found in crystal growing and glass, extrusion processes, paper industry, turbo-mechanics, thinning and drawing of copper wires, gas turbine rotors, polymer industry, lubrication processes, filtration process, and relevant to high-temperature nanomaterial processing technology.

2. Statement of the Problem

Unsteady transient three dimensional MHD viscous and an incompressible hybrid nanoparticles Ag-MoS_2 and Go-MoS_2 in hybrid base fluid $C_2H_6O_2$-H_2O (50–50%) flow over an extending sheet along with a rotating frame are considered as shown in Figure 1. The mathematical model is created through a species type that incorporates the chemical reactions and Arrhenius activation energy. The Buongiorno nanofluid model is implemented together with Tiwari and Das nanofluid model. Physically, we assume that the whole framework is at rest in the time $t < 0$ however for $t = 0$, the sheet is stretched along x-direction at $z = 0$ with angular velocity (Ω). B_0 is uniform (magnetic field) and applied along with z-direction, the incited magnetic field is ignored due to a small magnetic Reynolds number, and moreover, Ohmic dissipation and Hall's current impacts are ignored since the field of magnetic is not too much strong [40]. Moreover, the magnetic force acts normally to x and y-direction and no effect along z-direction as referred in schematic Figure 1. Further, we assume that

the thermo-physical properties of hybrid base, single and hybrid nanofluid along with shape factor are expressed in Table 1 and Table 2, the base fluid and nanoparticles are in thermal equilibrium and no slip occurs between them, and the agglomeration of nanoparticles is ignored because the hybrid nanofluid is synthesized as a stable compound. Furthermore, we assume that T_w, C_w are the surface temperature and concentration, respectively, and C_∞, T_∞ are the ambient concentration and temperature.
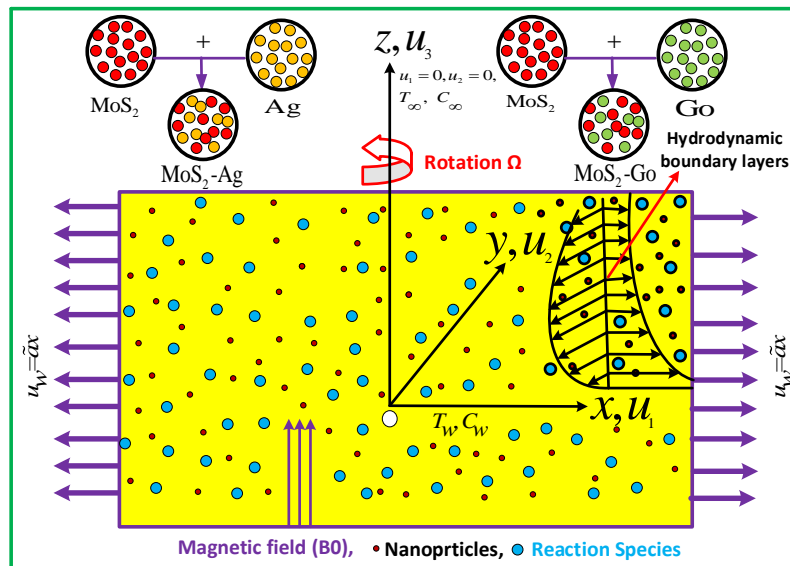
Figure 1. Schematic configuration with coordinate system.

3. Governing Equations

Considering the above suppositions, the consistent mass, momentum, energy, and conservation of concentration equations can be written as [41,42]:

$$\partial_x u_1 + \partial_y u_2 + \partial_z u_3 = 0, \tag{1}$$

$$\rho_{nf}(\partial_t u_1 + u_1 \partial_x u_1 + u_2 \partial_y u_1 + u_3 \partial_z u_1 - 2\Omega_1 u_2) = -\partial_x p + \mu_{nf}\partial_{zz}u_1 - \sigma_{nf}B_0^2 u_1, \tag{2}$$

$$\rho_{nf}(\partial_t u_2 + u_1 \partial_x u_2 + u_2 \partial_y u_2 + u_3 \partial_z u_2 - 2\Omega_1 u_1) = -\partial_y p + \mu_{nf}\partial_{zz}u_2 - \sigma_{nf}B_0^2 u_2, \tag{3}$$

$$\rho_{nf}(\partial_t u_3 + u_1 \partial_x u_3 + u_2 \partial_y u_3 + u_3 \partial_z u_3) = -\partial_z p + \mu_{nf}\partial_{zz}u_3, \tag{4}$$

$$\partial_t T + u_1 \partial_x T + u_2 \partial_y T + u_3 \partial_z T = \tilde{\alpha}_{nf}\partial_{zz}T + \tilde{\tau}^*\{\tilde{D}_B \partial_z C \partial_z T + \frac{\tilde{D}_T}{\tilde{T}_\infty}(\partial_z T)^2\}, \tag{5}$$

$$\partial_t C + u_1 \partial_x C + u_2 \partial_y C + u_3 \partial_z C = \tilde{D}_B \partial_{zz}C + \frac{\tilde{D}_T}{T_\infty}\partial_{zz}T - k_r^2(C - C\infty)\left(\frac{T}{T\infty}\right)^m \exp\left(\frac{-E_a}{k_B T}\right). \tag{6}$$

The Equation (1) represents the mass conservation for incompressible flow. On L.H.S of each of Equations (2)–(6), the local rate of change is described in the first terms, the second, the third, and fourth terms represents convection rate of change. The fifth term in Equations (2) and (3) shows the rotation. The first term on R.H.S of each of the Equations (2)–(4) indicates pressure gradient, the second term

corresponds to viscous effects and third term in Equations (2) and (3) signified the body force (magnetic effect). The right hand side of Equation (5), the first term is attributed with thermal diffusion and the second term exhibits the thermophoresis and Brownian motion phenomena. Similarly, on R.H.S of Equation (6), the first term stands for solutal diffusion, the second term for thermophoresis, and the last term in Equation (6), $k_r^2(C - C\infty)(\frac{T}{T\infty})^m exp(\frac{-E_a}{k_B T})$ shows the modified Arrhenius equation with a reaction rate of k_r^2 and fitted rate constant m. Here, u_1, u_2, and u_3 are velocity component in x, y, z directions, respectively, T and C are the fluid temperature and nanoparticle volume concentration, $\tilde{D}_B$ and $\tilde{D}_T$ are the Brownian diffusion and thermophoretic diffusion coefficient respectively, ρ_{nf}, $\tilde{\alpha}_{nf}$, μ_{nf}, and σ_{nf} are respectively the density, thermal diffusivity, dynamic viscosity, and electrical conductivity of the nanofluid. The current physical elaborated problem, characterized boundary conditions are [41,43]:

$$t < 0 : u_1 = 0, \ u_2 = 0, \ u_3 = 0, \ T = T_\infty, \ C = C_\infty, \tag{7}$$

$$t \geq 0 : u_1 = \tilde{a}x, u_2 = 0, u_3 = 0, \ T = T_w, C = C_w, \ as \ z = 0, \tag{8}$$

$$t \geq 0 : u_1 \to 0, \ u_2 \to 0, \ T \to T_\infty, \ C \to C_\infty, \ as \ z \to \infty. \tag{9}$$

In this current investigation, the authors attempted to utilize another way to enhance the technique of heat transfer in liquids, which is presently being talked about among researchers and scientists. The utilization of hybrid nanoparticles instead of single nanoparticles alongside the utilization of various shapes of nanoparticle and hybrid base liquid is adopted technique by the writers of this paper. Since hybrid nanoparticles thermal conductivity is greater than single nanoparticles thermal conductivity ($k_{hnf} > k_{nf}$), it is an ideal strategy for improving heat trasnferprocess in liquids. In Table 3, $\Phi = \Phi_1 + \Phi_2$ is the nanoparticles volume fraction and s_f is the nanoparticles shape factor, respectively.

Table 1. Thermo-physical properties of hybrid base fluid and nanoparticles [11,44].

Physical Properties	$C_2H_6O_2$-H_2O	MoS_2	Ag	Go
$\rho(kg \cdot m^3)$	1063.80	5060.0	10,490.0	1800.0
$C_p(J(kg \cdot °k))$	3630.00	397.21	235.000	717.0
$\sigma(\Omega \cdot m)$	9.75×10^{-4}	02.09×10^4	6.30×10^7	6.30×10^7
$\kappa(W(m \cdot °k)$	0.387	904.4	429	5000.0

We offer a following set of transformation variables to proceed the analysis (see [41,45,46]):

$$\left.\begin{array}{l} \eta = \sqrt{\dfrac{\tilde{a}x}{\zeta \nu_f}}z, \ f'(\zeta,\eta) = \dfrac{u_1}{\tilde{a}x_1}, \ g(\zeta,\eta) = \dfrac{u_2}{\tilde{a}x}, \ f(\zeta,\eta) = \dfrac{u_3}{-\sqrt{\tilde{a}\nu\zeta}}, \ \zeta = 1 - e^{-\tau}, \\[3mm] \tau = \tilde{a}t, \ \theta(\zeta,\eta)(T_w - T_\infty) = (T - T_\infty), \ \phi(\zeta,\eta)(C_w - C_\infty) = (C - C_\infty). \end{array}\right\} \tag{10}$$

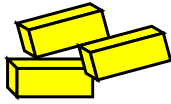**Table 2.** Nanoparticles shape with shape factor [47,48]

Nanoparticles Type	Shape	Shape Factor
Bricks		3.7
Cylinders		4.9
Platelets		5.7
Blades		8.9

Table 3. Thermo-physical properties of hybrid nanofluid [48,49].

Properties	Nanofluid	Hybrid Nanofluid
μ(viscosity)	$\mu_{nf} = \frac{\mu_f}{(1-\Phi)^{2.5}}$	$\mu_{hnf} = \frac{\mu_f}{(1-\Phi_1)^{2.5}(1-\Phi_2)^{2.5}}$
ρ(density)	$\rho_{nf} = \rho_f((1-\Phi) + \Phi\frac{\rho_s}{\rho_f}$	$\rho_{hnf} = \rho_f(1-\Phi_2)((1-\Phi_1) + \Phi_1\frac{\rho_{s1}}{\rho_f}) + \Phi_2\rho_{s2}$
ρC_p(Heat capacity)	$(\rho C_p)nf=(\rho C_p)_f((1-\Phi)+\Phi\frac{(\rho C_p)_s}{(\rho C_p)_f}$	$(\rho C_p)_{hnf}=(\rho C_p)_f(1-\Phi_2)((1-\Phi_1)+\Phi_1\frac{(\rho C_p)_{s1}}{(\rho C_p)_f})+\Phi_2(\rho C_p)_{s2}$
κ(Thermal conductivity)	$\frac{\kappa_{nf}}{\kappa_f} = \frac{\kappa_s+(s_f-1)\kappa_f-(s_f-1)\Phi(\kappa_f-\kappa_s)}{\kappa_s+(s_f-1)\kappa_f+\Phi(\kappa_f-\kappa_s)}$	$\frac{\kappa_{hnf}}{\kappa_{bf}} = \frac{\kappa_{s2}+(s_f-1)\kappa_{bf}-(s_f-1)\Phi_2(\kappa_{bf}-\kappa_{s2})}{\kappa_{s2}+(s_f-1)\kappa_{bf}+\Phi(\kappa_{bf}-\kappa_{s2})}$ where $\frac{\kappa_{bf}}{\kappa_f} = \frac{\kappa_{s1}+(s_f-1)\kappa_f-(s_f-1)\Phi_1(\kappa_f-\kappa_{s1})}{\kappa_{s1}+(s_f-1)\kappa_f+\Phi(\kappa_f-\kappa_{s1})}$
σ(Electrical conductivity)	$\frac{\sigma_{nf}}{\sigma_f} = 1 + \frac{3(\sigma-1)\Phi}{(\sigma+2)-(\sigma-1)\Phi}$	$\frac{\sigma_{hnf}}{\sigma_{bf}} = 1 + \frac{3\Phi(\sigma_1\Phi_1+\sigma_2\Phi_2-\sigma_{bf}(\Phi_1+\Phi_2))}{(\sigma_1\Phi_1+\sigma_2\Phi_2+2\Phi\sigma_{bf})-\Phi\sigma_{bf}((\sigma_1\Phi_1+\sigma_2\Phi_2)-\sigma_{bf}(\Phi_1+\Phi_2))}$

The continuity Eqaution (1) is satisfied identically using above similarity transformations. In light of Eqaution (10), the Eqautions (2)–(9) reduce into following non-linear PDEs in the transformed coordinate system (ζ, η).

$$\frac{1}{\chi_1\chi_2}f''' + \frac{1}{2}(1-\zeta)\eta f'' + \zeta(f'' - f'^2 + 2\lambda g - \frac{\chi_3}{\chi_2}M^2 f') = \zeta(1-\zeta)\frac{\partial f'}{\partial \zeta}, \tag{11}$$

$$\frac{1}{\chi_1\chi_2}g'' + \frac{1}{2}(1-\zeta)\eta g' + \zeta(fg' - f'g - 2\lambda f' - \frac{\chi_3}{\chi_2}M^2 g) = \zeta(-\zeta)\frac{\partial g}{\partial \zeta}, \tag{12}$$

$$\frac{\chi_4}{\chi_5}\theta'' + \frac{1}{2}(1-\zeta)\eta Pr\theta' + Pr\zeta f\theta' + NbPr\theta\phi + NtPr\theta'^2 = Pr\zeta(1-\zeta)\frac{\partial \theta}{\partial \zeta}, \tag{13}$$

$$\phi'' + \frac{Le}{2}(1-\zeta)\eta\phi' + Le\zeta f\phi' + \frac{Nt}{Nb}\theta'' - Le\Gamma\zeta(1+\delta\theta)^m \exp(-\frac{EE}{1+\delta\theta})\phi = Le\zeta(1-\zeta)\frac{\partial \phi}{\partial \zeta}, \tag{14}$$

$$f(\zeta,\eta) = 0, \; f'(\zeta,\eta) = 1, \; g(\zeta,\eta) = 0, \; \theta(\zeta,\eta) = 1, \; \phi(\zeta,\eta) = 1, \; \zeta \geq= 0, \; at \; \eta = 0, \Big\}$$
$$f'(\zeta,\infty) \to 0, \; g(\zeta,\infty) \to 0, \; \theta(\zeta,\infty) \to 0, \; \phi(\zeta,\infty) \to 0, \; \zeta \geq 0, \; as \; \eta \to \infty. \Big\} \tag{15}$$

where

$$\chi_1 = (1-\Phi_1)^{2.5}(1-\Phi_2)^{2.5}, \chi_2 = (1-\Phi_2)\left\{(1-\Phi_1) + \Phi_1\frac{\rho_{s1}}{\rho_f}\right\} + \Phi_2\frac{\rho_{s2}}{\rho_f},$$

$$\chi_3 = \left\{1 + \frac{3(s_f-1)(\frac{\sigma_2}{\sigma_f}-1)\Phi_2}{(\frac{\sigma_2}{\sigma_f}+2)-(\frac{\sigma_2}{\sigma_f}-1)(s_f-1)\Phi_2} + \frac{3(s_f-1)(\frac{\sigma_1}{\sigma_f}-1)\Phi_1}{(\frac{\sigma_1}{\sigma_f}+2)-(\frac{\sigma_1}{\sigma_f}-1)(s_f-1)\Phi_1}\right\}\sigma_f,$$

$$\chi_4 = \frac{\kappa_{s2}+(s_f-1)\kappa_{bf}-(s_f-1)\Phi_2(\kappa_{bf}-\kappa_{s2})}{\kappa_{s2}+(s_f-1)\kappa_{bf}+\Phi_2(\kappa_{bf}-\kappa_{s2})} \cdot \frac{\kappa_{s1}+(s_f-1)\kappa_f-(s_f-1)\Phi_1(\kappa_f-\kappa_{s1})}{\kappa_{s1}+(s_f-1)\kappa_f+\Phi_1(\kappa_f-\kappa_{s1})},$$

$$\chi_5 = (1-\Phi_2)\left\{(1-\Phi_1) + \Phi_1\frac{\rho_{s1}}{\rho_f}\right\} + \Phi_2\frac{\rho_{s2}}{\rho_f}.$$

and primes $('','',''')$ denote the d.r.t η. The come into view parameters in Eqautions (11)–(14) are defined as:

$$\lambda = \frac{\Omega_1}{\tilde{a}}, \; M = \sqrt{\frac{\sigma_f B_o^2}{\rho_f \tilde{a}}}, \; Pr = \frac{\nu_f(\rho C_p)_f}{\kappa_f}, \; Le = \frac{\nu}{\tilde{D}_B}, \; Nb = \nu^{-1}\tilde{\tau}^* \tilde{D}_B(\tilde{C}_w - \tilde{C}_\infty),$$

$$Nt = \frac{\tilde{\tau}^* \tilde{D}_T(\tilde{T}_w - \tilde{T}_\infty)}{\nu \tilde{T}_\infty}, \; \Gamma = \frac{k_r^2}{a}, \; \delta = \frac{T_w - T_\infty}{T_\infty}, \; EE = \frac{E_a}{\kappa_B T_\infty}.$$

where λ, M, Pr, Le, Nb, Nt, Γ, δ, and EE are the rotating parameter, magnetic parameter, Prandtl number, Lewis number, Brownian motion, thermophoresis parameter, chemical reaction rate, temperature difference, and activation energy respectively. When $\tau \to \infty$, $\zeta = 1$, then the Eqautions (11)–(14) become:

$$\frac{1}{\chi_1\chi_2}f''' + ff'' - f'^2 + 2\lambda g - \frac{\chi_3}{\chi_2}M^2 f' = 0, \tag{16}$$

$$\frac{1}{\chi_1\chi_2}g'' + fg' - f'g - 2\lambda f' - \frac{\chi_3}{\chi_2}M^2 g = 0, \tag{17}$$

$$\frac{\chi_4}{\chi_5}\theta'' + Prf\theta' + NbPr\theta\phi + NtPr\theta'^2 = 0, \tag{18}$$

$$\phi'' + Lef\phi' + \frac{Nt}{Nb}\theta'' - Le\Gamma(1+\delta\theta)^m \exp(-\frac{EE}{1+\delta\theta})\phi = 0. \tag{19}$$

subject to the boundary conditions (15)

Skin friction coefficient expressions, local Nusselt number, and Sherwood number are defined as:

$$Cf_x = \frac{\tau_w^x}{\rho\tilde{u}_1^2}, \; Cf_y = \frac{\tau_w^y}{\rho\tilde{u}_1^2}, \; Nu = \frac{xq_w}{\kappa(\tilde{T}_w - \tilde{T}_\infty)}, \; Shr = \frac{xq_m}{\tilde{D}_B(\tilde{C}_w - \tilde{C}_\infty)}. \tag{20}$$

where the skin friction tensor at wall are $\tau_w^x = \mu_{nf}(\partial u_1/\partial z)_{z=0}$ (x-direction) and $\tau_w^y = \mu_{nf}(\partial u_2/\partial z)_{z=0}$ (y-direction), the wall heat transfer is $q_w = -\kappa_{nf}(\partial \tilde{T}_1/\partial z_1)_{z_1=0}$, and the mass flux from the sheet is $q_m = -\tilde{D}_B(\partial \tilde{C}_1/\partial z_1)_{z_1=0}$. By the aid of similarity transformation Equation (10), we get

$$
\begin{cases}
Cf_x Re_x^{1/2} = \dfrac{f''(0)}{\chi_1\chi_2\sqrt{\zeta}}, Cf_y Re_x^{1/2} = \dfrac{h'(0)}{\chi_1\chi_2\sqrt{\zeta}}, \\
Nu_x Re_x^{1/2} = -\dfrac{[\chi_4\theta'(0)]}{\sqrt{\zeta}}, Shr_x Re_x^{1/2} = -\dfrac{[\phi'(0)]}{\sqrt{\zeta}}.
\end{cases}
\tag{21}
$$

4. Finite Element Method Solutions

The set of PDEs (partial differential equations) Equations (11)–(14) cannot be solved analytically due to highly non-linearity. The transformed set of non-linear PDEs Equations (11)–(14) is solved numerically utilizing the variational finite element method along with boundary conditions (Eqaution (15)). This technique is an excellent numerical computational strategy valuable to solve the different real word and engineering analysis problems such as fluids with heat transfer, structural engineering, Bio-materials, chemical processing, rigid body dynamics, and different territories [50]. In present-day engineering analysis, it tends to be applied for solving integral equations and amazingly efficient technique to solve various nonlinear problems [51–54]. Reddy [55] outlined an excellent general description of the variational finite elements method and [56] summarized the basic steps involved in the FEM. Basically the technique is comprised of continuous piecewise function for the solution and to get the function's parameters in a systematic manner that minimizes the error [57]. The FEM solves boundary value problem adequately, rapidly and precisely [58,59]. To reduce the order of nonlinear differential Equations (11)–(15), firstly we consider:

$$
f' = q,
\tag{22}
$$

The set of Eqautions (11)–(15) thus reduces to

$$
\frac{1}{\chi_1\chi_2}q'' + \frac{1}{2}(1-\zeta)\eta q' + \zeta(fq' - q^2 + 2\lambda g - \frac{\chi_3}{\chi_2}M^2 q) = \zeta(1-\zeta)\frac{\partial q}{\partial \zeta},
\tag{23}
$$

$$
\frac{1}{\chi_1\chi_2}g'' + \frac{1}{2}(1-\zeta)\eta g' + \zeta(fg' - qg - 2\lambda q - \frac{\chi_3}{\chi_2}M^2 g) = \zeta(1-\zeta)\frac{\partial g}{\partial \zeta},
\tag{24}
$$

$$
\frac{\chi_4}{\chi_5}\theta'' + \frac{1}{2}(1-\zeta)Pr\eta\theta' + Pr\zeta f\theta' + NbPr\theta'\phi' + NtPr\theta'^2 = Pr\zeta(1-\zeta)\frac{\partial \theta}{\partial \zeta},
\tag{25}
$$

$$
\phi'' + \frac{Le}{2}(1-\zeta)\eta\phi' + Le\zeta f\phi' + \frac{Nt}{Nb}(\theta'')^2 - Le\Gamma\zeta(1+\delta\theta)^m \exp(-\frac{EE}{1+\delta\theta})\phi = Le\zeta(1-\zeta)\frac{\partial \phi}{\partial \zeta},
\tag{26}
$$

$$
\left.\begin{aligned}
f(\zeta,\eta) = q(\zeta,\eta) = g(\zeta,\eta) = 0, \ \theta(\zeta,\eta) = \phi(\zeta,\eta) = 1, \quad at \quad \eta = 0, \\
q(\zeta,\eta) \to 0, \ g(\zeta,\eta) \to 0, \ \theta(\zeta,\eta) \to 0, \ \phi(\zeta,\eta) \to 0, \ as \ \eta \to \infty.
\end{aligned}\right\}
\tag{27}
$$

4.1. Variational Formulations

Over a typical rectangular element Ω_e, the associated variational form with Eqautions (22)–(26) is given by

$$\int_{\Omega_e} w_{f2}\left\{\frac{1}{\chi_1\chi_2}q'' + \frac{1}{2}(1-\zeta)\eta q' + \zeta(fq' - q^2 + 2\lambda g - \frac{\chi_3}{\chi_2}M^2 q) - \zeta(1-\zeta)\frac{\partial q}{\partial \zeta}\right\}d\Omega_e = 0, \quad (28)$$

$$\int_{\Omega_e} w_{f3}\left\{\frac{1}{\chi_1\chi_2}g'' + \frac{1}{2}(1-\zeta)\eta g' + \zeta(fg' - qg - 2\lambda q - \frac{\chi_3}{\chi_2}M^2 g) - \zeta(1-\zeta)\frac{\partial g}{\partial \zeta}\right\}d\Omega_e = 0, \quad (29)$$

$$\int_{\Omega_e} w_{f4}\left\{\frac{\chi_4}{\chi_5}\theta'' + \frac{Pr}{2}(1-\zeta)\eta\theta' + Pr\zeta f\theta' + NbPr\theta'\phi' + NtPr\theta'^2 - Pr\zeta(1-\zeta)\frac{\partial\theta}{\partial\zeta}\right\}d\Omega_e = 0, \quad (30)$$

$$\int_{\Omega_e} w_{f5}\left\{\phi'' + \frac{Le}{2}(1-\zeta)\eta\phi' + Le\zeta f\phi' + \frac{Nt}{Nb}\theta''^2 - Le\zeta(1-\zeta)\frac{\partial\phi}{\partial\zeta}\right.$$

$$\left. - Le\Gamma\zeta(1+\delta\theta)^m \exp(-\frac{EE}{1+\delta\theta})\phi\right\}d\Omega_e = 0. \quad (31)$$

where $w_{fs}(s = 1, 2, 3, 4, 5)$ are arbitrary weight functions or trial functions.

4.2. Finite Element Formulations

Let it divide the rectangular domain (Ω_e) into 4-noded (rectangular element) and (ζ_i, η_j) be the domain grid points (see Figure 2). The length of plate and thickness of boundary layer is fixed at $\zeta_{max} = 1$, $\eta_{max} = 5$, respectively. The finite model of the element can be obtained from Equations (28)–(31) by replacing the following form of finite element approximations:

$$f = \sum_{j=1}^{4} f_j\Psi_j(\zeta,\eta), \; q = \sum_{j=1}^{4} q_j\Psi_j(\zeta,\eta), \; g = \sum_{j=1}^{4} g_j\Psi_j(\zeta,\eta), \; \theta = \sum_{j=1}^{4} \theta_j\Psi_j(\zeta,\eta), \; \phi = \sum_{j=1}^{4} \phi_j\Psi_j(\zeta,\eta). \quad (32)$$

here, Ψ_j (j = 1, 2, 3, 4) are the linear interpolation functions for a rectangular element Ω_e (see Figure 2) and are given by:

$$\Psi_1 = \frac{(\zeta_{e+1} - \zeta)(\eta_{e+1} - \eta)}{(\zeta_{e+1} - \zeta_e)(\eta_{e+1} - \eta_e)}, \quad \Psi_2 = \frac{(\zeta - \zeta_e)(\eta_{e+1} - \eta)}{(\zeta_{e+1} - \zeta_e)(\eta_{e+1} - \eta_e)},$$

$$\Psi_3 = \frac{(\zeta - \zeta_e)(\eta - \eta_e)}{(\zeta_{e+1} - \zeta_e)(\eta_{e+1} - \eta_e)}, \quad \Psi_4 = \frac{(\zeta_{e+1} - \zeta)(\eta - \eta_e)}{(\zeta_{e+1} - \zeta_e)(\eta_{e+1} - \eta_e)}. \quad (33)$$

the model of finite elements of the equations thus developed is given by:

$$\begin{bmatrix} [L^{11}] & [L^{12}] & [L^{13}] & [L^{14}] & [L^{15}] \\ [L^{21}] & [L^{22}] & [L^{23}] & [L^{24}] & [L^{25}] \\ [L^{31}] & [L^{32}] & [L^{33}] & [L^{34}] & [L^{35}] \\ [L^{41}] & [L^{42}] & [L^{43}] & [L^{44}] & [L^{45}] \\ [L^{51}] & [L^{52}] & [L^{53}] & [L^{54}] & [L^{55}] \end{bmatrix} \begin{bmatrix} \{f\} \\ \{q\} \\ \{h\} \\ \{\theta\} \\ \{\phi\} \end{bmatrix} = \begin{bmatrix} \{r_1\} \\ \{r_2\} \\ \{r_3\} \\ \{r_4\} \\ \{r_5\} \end{bmatrix} \quad (34)$$

where $[W_{mn}]$ and $[b_m]$ (m, n = 1, 2, 3, 4, 5) are defined as:

$$L_{ij}^{11} = \int_{\Omega_e} \Psi_i \frac{d\Psi_j}{d\eta} d\Omega_e, \ L_{ij}^{12} = -\int_{\Omega_e} \Psi_i \Psi_j d\Omega_e, \ L_{ij}^{13} = L_{ij}^{14} = L_{ij}^{15} = L_{ij}^{21} = 0$$

$$L_{ij}^{22} = -\frac{1}{\chi_1\chi_2} \int_{\Omega_e} \frac{d\Psi_i}{d\eta} \frac{d\Psi_j}{d\eta} d\Omega_e + \frac{1}{2}(1-\zeta)\eta \int_{\Omega_e} \Psi_i \frac{d\Psi_j}{d\eta} d\Omega_e + \zeta \int_{\Omega_e} \bar{f}\Psi_i \frac{d\Psi_j}{d\eta} d\Omega_e - \zeta \int_{\Omega_e} \bar{q}\Psi_i \Psi_j d\Omega_e$$

$$- \frac{\zeta_3}{\zeta_2} M^2 \int_{\Omega_e} \zeta\Psi_i \Psi_j d\Omega_e - \zeta(1-\zeta)\int_{\Omega_e} \Psi_i \frac{d\Psi_j}{d\zeta} d\Omega_e, \ L_{ij}^{23} = -2\lambda\zeta \int_{\Omega_e} \Psi_i \Psi_j d\Omega_e, \ L_{ij}^{24} = L_{ij}^{25} = W_{ij}^{31} = 0,$$

$$W_{ij}^{32} = -2\lambda\zeta \int_{\Omega_e} \Psi_i \Psi_j d\Omega_e,$$

$$L_{ij}^{33} = -\frac{1}{\chi_1\chi_2} \int_{\Omega_e} \frac{d\Psi_i}{d\eta} \frac{d\Psi_j}{d\eta} d\Omega_e + \frac{1}{2}(1-\zeta)\eta \int_{\Omega_e} \Psi_i \frac{d\Psi_j}{d\eta} d\Omega_e + \zeta \int_{\Omega_e} \bar{f}\Psi_i \frac{d\Psi_j}{d\eta} d\Omega_e - \zeta \int_{\Omega_e} \bar{q}\Psi_i \Psi_j d\Omega_e$$

$$- \frac{\chi_3}{\chi_2} M^2 \int_{\Omega_e} \zeta\Psi_i \Psi_j d\Omega_e - \zeta(1-\zeta)\int_{\Omega_e} \Psi_i \frac{d\Psi_j}{d\zeta} d\Omega_e, \ L_{ij}^{34} = L_{ij}^{35} = L_{ij}^{41} = L_{ij}^{42} = L_{ij}^{43} = 0,$$

$$L_{ij}^{44} = -\frac{\chi_4}{\chi_5} \int_{\Omega_e} \frac{d\Psi_i}{d\eta} \frac{d\Psi_j}{d\eta} d\Omega_e + \frac{Pr}{2}(1-\zeta)\eta \int_{\Omega_e} \Psi_i \frac{d\Psi_j}{d\eta} d\Omega_e + Pr\zeta \int_{\Omega_e} \bar{f}\Psi_i \frac{d\Psi_j}{d\eta} d\Omega_e + PrNb \int_{\Omega_e} \bar{\phi}'\Psi_i \frac{d\Psi_j}{d\eta} d\Omega_e$$

$$+ PrNt \int_{\Omega_e} \bar{\theta}'\Psi_i \frac{d\Psi_j}{d\eta} d\Omega_e - Pr\zeta(1-\zeta)\int_{\Omega_e} \Psi_i \frac{d\Psi_j}{d\zeta} d\Omega_e, \ L_{ij}^{45} = L_{ij}^{51} = L_{ij}^{52} = 0,$$

$$L_{ij}^{53} = -\frac{Nt}{Nb} \int_{\Omega_e} \frac{d\Psi_i}{d\eta} \frac{d\Psi_j}{d\eta} d\Omega_e, \ L_{ij}^{55} = -\int_{\Omega_e} \frac{d\Psi_i}{d\eta} \frac{d\Psi_j}{d\eta} d\Omega_e + \frac{Le}{2}(1-\zeta)\eta \int_{\Omega_e} \Psi_i \frac{d\Psi_j}{d\eta} d\Omega_e$$

$$+ Le\zeta \int_{\Omega_e} \bar{f}\Psi_i \frac{d\Psi_j}{d\eta} d\Omega_e - Le\zeta(1-\zeta)\int_{\Omega_e} \Psi_i \frac{d\Psi_j}{d\zeta} d\Omega_e - \int_{\Omega_e} (1+\gamma\bar{\theta})^m \exp(\frac{-EE}{1+\gamma\bar{\theta}})\Psi_i \Psi_j d\Omega_e$$

and

$$r_i^1 = 0, \ r_i^2 = -\frac{1}{\chi_1\chi_2} \oint_{\Gamma_e} \Psi_i n_\eta \frac{\partial q}{\partial \eta} ds, \ r_i^3 = -\frac{1}{\chi_1\chi_2} \oint_{\Gamma_e} \Psi_i n_\eta \frac{\partial g}{\partial \eta} ds, \ r_i^4 = -\frac{\chi_4}{\chi_5} \oint_{\Gamma_e} \Psi_i n_\eta \frac{\partial \theta}{\partial \eta} ds,$$

$$r_i^5 = -\oint_{\Gamma_e} \Psi_i n_\eta \frac{\partial \phi}{\partial \eta} ds - \frac{Nt}{Nb} \oint_{\Gamma_e} \Psi_i n_\eta \frac{\partial \theta}{\partial \eta} ds. \tag{35}$$

where, the known values are to be considered $\bar{f} = \sum_{j=1}^4 \bar{f}_j\Psi_j$, $\bar{q} = \sum_{j=1}^4 \bar{q}_j\Psi_j$, $\bar{g} = \sum_{j=1}^4 \bar{g}_j\Psi_j$, $\bar{\theta}' = \sum_{j=1}^4 \bar{\theta}'_j\Psi_j$, and $\bar{\phi}' = \sum_{j=1}^4 \bar{\phi}'_j\Psi_j$. The flow domain is divided into 101×101 rectangular elements of similar size of grid points. Five functions can be assessed at each node, and 51, 005 equations are obtained after assembly of all element equations. The obtained equations are non-linear after applying boundary conditions which are solved by utilizing the Newton–Raphson method with the required precision of 0.000005.
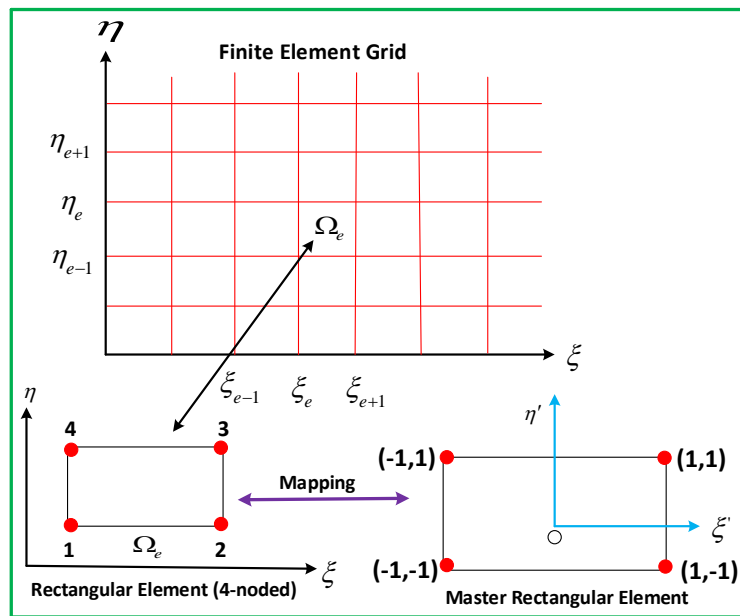
Figure 2. Finite element grid and finite element mesh of rectangular element.

5. Results and Discussion

The outcomes of this work are evaluated by solving the transformed two dimensional PDEs (Eqautions (11))–(14)) along with initial and boundary conditions (Eqaution (15)). This set of non linear equations involves four dependent variables f', g, θ and ϕ and two independent variables ζ, η. A variational finite element simulation is performed for suitable ranges of the influential entities that help to understand the varying behaviors of the physical quantities. Before plotting the outcomes, we have approved our outcomes with the already published research articles through Tables 4–6. An excellent coincidence has been achieved which confirms the accuracy of the FEM Matlab code. The estimation of present analysis is made by putting the values for involved parameters: Nb = 0.3, Nt = 0.3, $\lambda = 1.0$, $Pr = 6.2$ (water-based nanofluid), $M = 1.0$, $Le = 10.0$, $S_f = 2.0$, $\Phi_1 = \Phi_2 = 0.2$.

Table 4. $g'(0)$ and $f''(0)$ value along with diverse values of λ at $\zeta = 1$ when remaining parameters are zeros.

λ	Nazar et al. [32]		Wang [30]		FEM (Our Results)	
	$-f''(0)$	$-h'(0)$	$-f''(0)$	$-h'(0)$	$-f''(0)$	$-h'(0)$
0.0	1.0000	0.0000	1.0000	0.0000	1.00000	0.00000
0.5	1.1384	0.5128	1.1384	0.5128	1.13844	0.51283
1.0	1.3250	0.8371	1.3250	0.8371	1.32501	0.83715
2.0	1.6523	1.2873	1.6523	1.2873	1.65232	1.28732
5.0	-	-	-	-	2.39026	2.15024

Table 5. $-\theta'(0)$ value along with diverse values of λ at $\zeta = 1$ when remaining parameters are zeros.

λ	Adnan et al. [60]			FEM (Our Results)		
	Pr = 0.7	Pr = 2.0	Pr = 7.0	Pr = 0.7	Pr = 2.0	Pr = 7.0
0.0	0.455	0.911	1.894	0.4552	0.9108	1.8944
0.5	0.390	0.853	1.850	0.3901	0.8525	1.8500
1.0	0.321	0.770	1.788	0.3214	0.7703	1.7877
2.0	0.242	0.638	1.664	0.2420	0.6381	1.6642

Table 6. $-\theta'(0)$ value along with diverse values of λ at $\zeta = 1$ and $Pr = 2.0$ when remaining parameters are zeros.

λ	Abbas et al. [41]			FEM (Our Results)		
	M = 0.5	**M = 1.0**	**M = 2.0**	**M = 0.5**	**M = 1.0**	**M = 2.0**
0.0	0.886	0.823	0.668	0.8862	0.8230	0.6682
0.5	0.841	0.800	0.663	0.8408	0.8003	0.6627
1.0	0.768	0.750	0.648	0.7684	0.7501	0.6483
2.0	0.641	0.643	0.603	0.6411	0.6429	0.6030
5.0	0.447	0.449	0.461	0.4467	0.4494	0.4612

The impact of magnetic parameter M on primary velocity f', secondary velocity g, temperature θ and nanoparticle concentration ϕ is plotted respectively in Figure 3a–d. It is revealed that velocity component $f'(\zeta, \eta)$ decreases monotonically and the magnitude of velocity component $g(\zeta, \eta)$ diminishes significantly when parameter M is incremented. This depreciation in the velocities is associated with the enhancement in the resistive force known as Lorentz force which is produced during the interaction of magnetic and electric fields. This phenomenon helps to control the boundary layer thickness. It is also seen that cross-flow effects create reverse flow. The flow along the x-axis seems to dominate the reverse flow because of the stretch in boundary but the reverse flow prevails in the y-direction and the velocity $g(\zeta, \eta)$ attains negative values. It is also observed that velocity $f'(\zeta, \eta)$ is slightly faster for hybrid phase Go-MoS$_2$ than hybrid phase Ag-MoS$_2$ but the velocity $g(\zeta, \eta)$ presents contrary behavior for the two nano phases. Figure 3c exhibits a monotonic increase in temperature $\theta(\zeta, \eta)$ with the progressive strength of parameter M. This is because the flow is halted and the dissipation adds to the thermal energy of nano liquids. Figure 3d illustrates the steadily rising trend of nanoparticle concentration $\phi(\zeta, \eta)$ with exceeding values of M. The concentration values for hybrid nano liquids Go-MoS$_2$ is lesser as compared with that of hybrid liquids Ag-MoS$_2$.
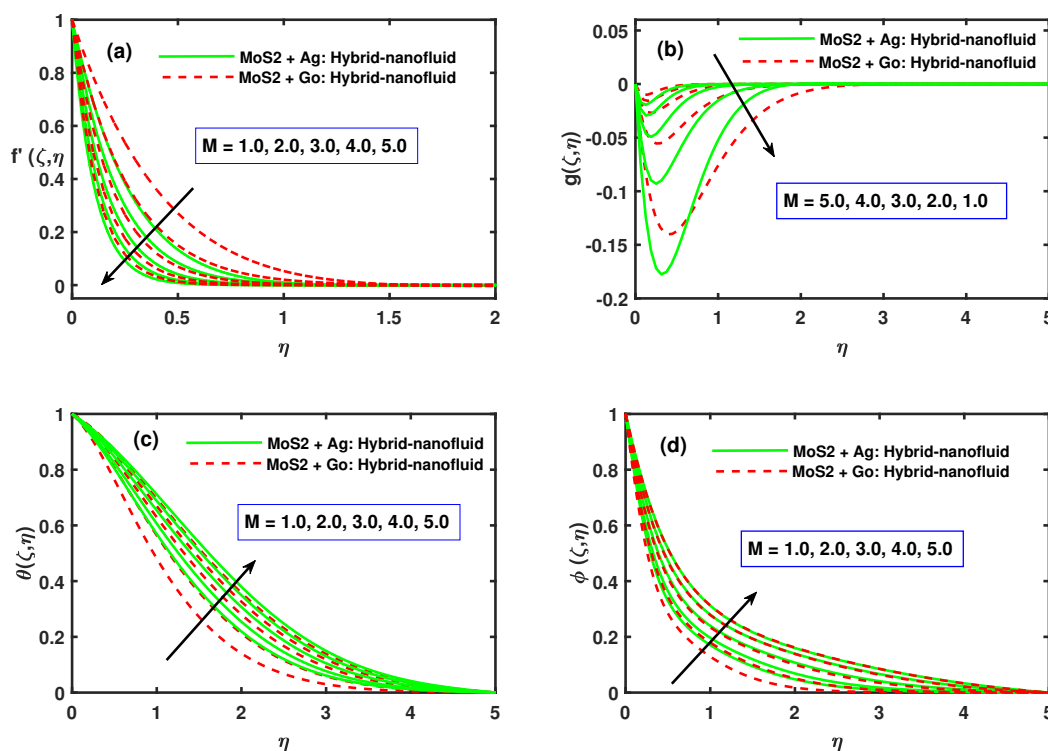

Figure 3. Fluctuation of $f'(\zeta, \eta)$, $g(\zeta, \eta)$, $\theta(\zeta, \eta)$, and $\phi(\zeta, \eta)$ along with M (magnetic field) at $\zeta = 1$.

Figures 4a,b are sketched to describe the retarding impacts of rotational parameter lambda on velocity components $f'(\zeta, \eta)$ and $g(\zeta, \eta)$. There is significant decrease in f' against the parameter λ, this velocity attains its peak value when $\lambda = 0$ (no rotation). The plots for $g(\zeta, \eta)$ acquire negative orientation and oscillatory patterns and its magnitude goes on decreasing when the input values of λ become higher. This bidirectional decelerated motion of nano liquids is a consequence of Coriolis forces $2\zeta\lambda g$ and $-2\zeta\lambda f'$ incorporated respectively in Eqautions (11) and (12). The two terms are negative (because $g < 0$) and thus they offer resistance to the flow. However, the resistive force along the horizontal direction is overcome by the stretching effect and a meager fluctuation in $f'(\zeta, \eta)$ occurs away from the sheet but the velocity $g(\zeta, \eta)$ is influenced significantly with prominent fluctuations under the opposing force in the y-direction. The temperature of nano liquids $\theta(\zeta, \eta)$ and nanoparticle concentration $\phi(\zeta, \eta)$ are enhanced directly with incremental values of λ as depicted from Figure 4c,d. The development in thermal and concentration boundary layers is justified on the basis of enhanced diffusion processes due to increased rotation.
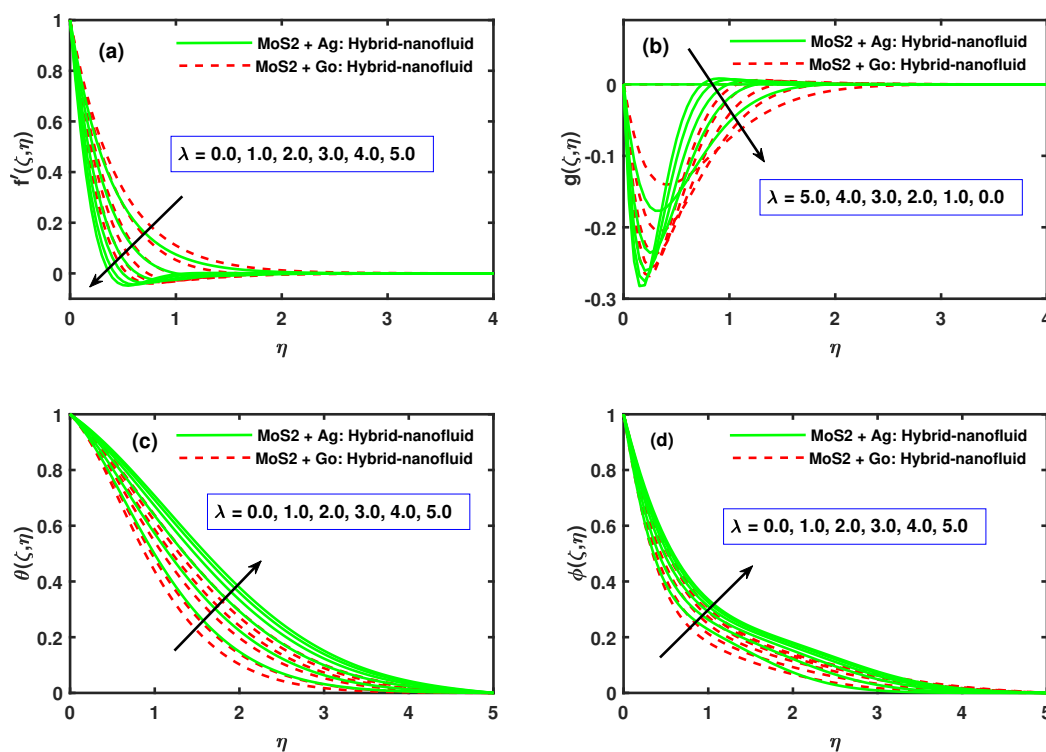

Figure 4. Fluctuation of $f'(\zeta, \eta)$, $g(\zeta, \eta)$, $\theta(\zeta, \eta)$, and $\phi(\zeta, \eta)$ along with λ (rotating parameter) at $\zeta = 1$.

From the Figure 5a,b, it is manifested that velocity curves for $f'(\zeta, \eta)$ and $g(\zeta, \eta)$ decline against the incremented variation of unsteady parameter τ. Figure 5c demonstrate temperature escalation with improved values of τ. The nanoparticle concentration $\phi(\zeta, \eta)$ undergoes a fluctuating distribution with increment in τ as illustrated from Figure 5d. It recedes near the plane sheet when $\eta < 1$, then it increases for $\eta = 3$. Figure 6a,b reveal that the monotonic increase in nano liquid temperature distribution is established when Brownian motion parameter Nb and thermophoresis parameter Nt are progressed. Actually, these two factors are of fundamental importance for the nanofluid model. Thermophoresis implies the movement of nanoparticles from hot to cold segments of nano liquid and Brownian motion exemplify the random motion of nanoparticles. Thus both the parameters contribute to diffusion processes and hence raise the temperature.
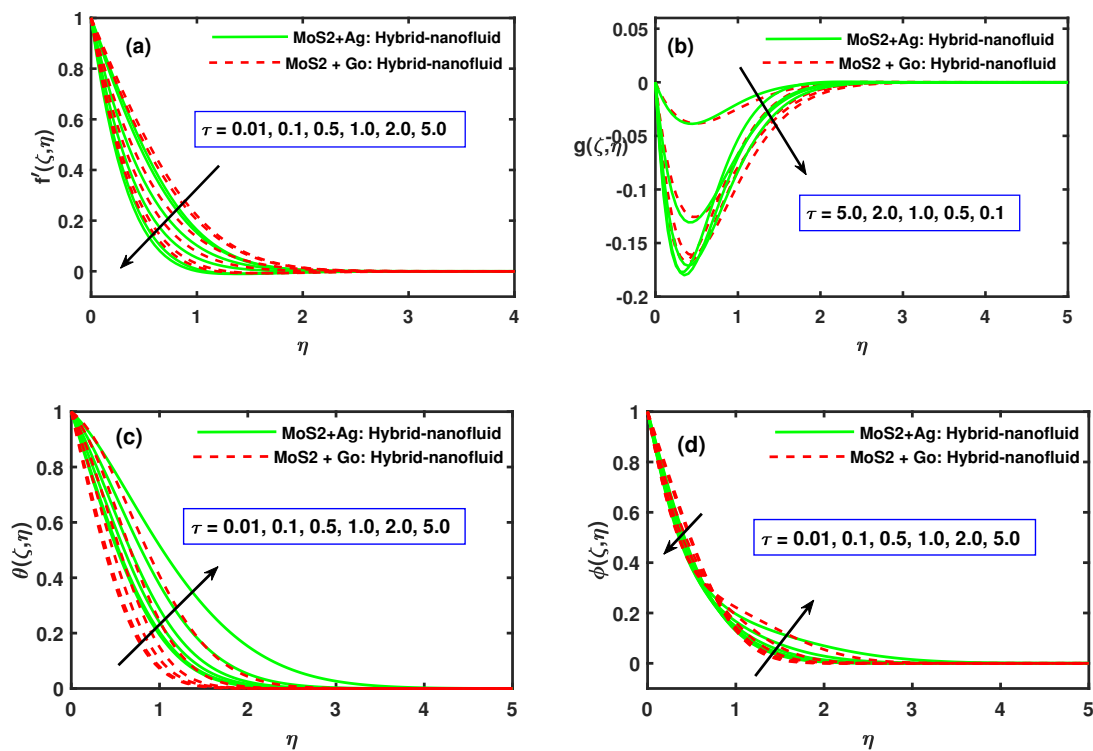
Figure 5. Fluctuation of $f'(\zeta,\eta)$, $g(\zeta,\eta)$, $\theta(\zeta,\eta)$, and $\phi(\zeta,\eta)$ along with τ (unsteady parameter) at $\zeta = 1$.
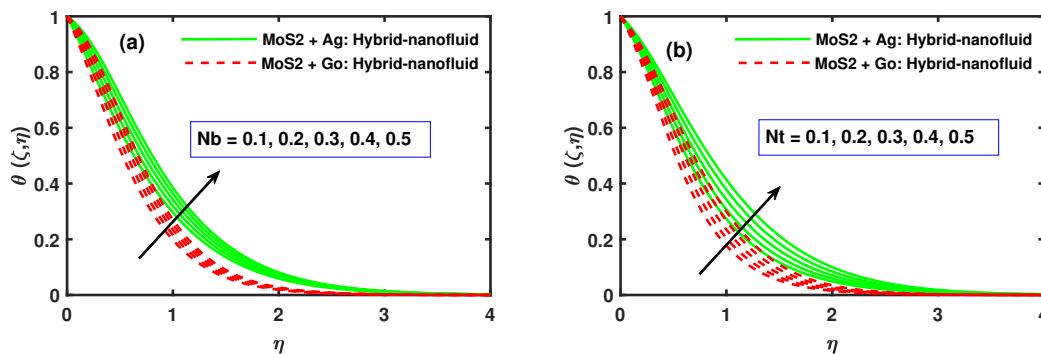

Figure 6. Fluctuation of $\theta(\zeta,\eta)$ along with Nb (Brownian motion) and Nt (thermophoresis) at $\zeta = 1$.

In the same way, the shape function S_f and nanoparticle volume fraction Φ_2 have also raised the temperature $\theta(\zeta,\eta)$ as sketched in Figure 7a,b. Further, it is seen that the factor S_f has marked significant impact on $\theta(\zeta,\eta)$. It is mentionable that temperature for hybrid nano liquids Ag-MoS$_2$ attains higher values than the hybrid-nano fluid Go-MoS$_2$ for all cases discussed above. This finding is a manifestation of our principal objective for the current study. Physically, thermal conductivity is enhanced for hybrid nanofluids Ag-MoS$_2$ than the hybrid-nano fluids Go-MoS$_2$ and hence the efficient thermal transportation can be acquired to meet the growing need of various techno processes.

Figure 8a,b discloses that nanoparticle concentration $\phi(\zeta,\eta)$ develops meagerly near the boundary of sheet ($\eta = 0.5$), then it rises vividly within boundary layer ($\eta > 0.5$) against Nt. It is also noticed that nanoparticle concentration $\phi(\zeta,\eta)$ reduces monotonically when Lewis number Le attains higher input. The reason for this outcome lies in the fact that Lewis's number is reciprocal to Brownian diffusion and hence its larger values are responsible to reduce the diffusion of nanoparticles. Moreover, the nanoparticle concentration for hybrid phase Go-MoS$_2$ is lesser than that of hybrid phase Ag-MoS$_2$.

The incremented activation energy parameter (EE) boosts the concentration $\phi(\zeta, \eta)$ as displaced in Figure 9a. In addition, Figure 9b is presented to disclose the lowering of concentration $\phi(\zeta, \eta)$ when the chemical reaction parameter Γ is allotted higher input values.

Figure 10a,b demonstrate the variation of the coefficients of skin friction ($Cf_x Re_x^{1/2}, Cf_y Re_y^{1/2}$) along x- and y- directions respectively under the variation of ζ and λ and the Figure 11a,b depict these quantities against magnetic parameter M and ζ. One can notice that for exceeding λ and M the skin friction coefficients in both the directions are augmented notably for $\zeta < 0.15$ and for $\zeta > 0.15$ (nearly) these quantities become uniform for a given λ and M. However, the quantity $Cf_y Re_y^{1/2}$ undergoes some fluctuation for larger values of λ but it remains smooth for varying values of M. It means the application of magnetic field provides sufficient control to the flow.
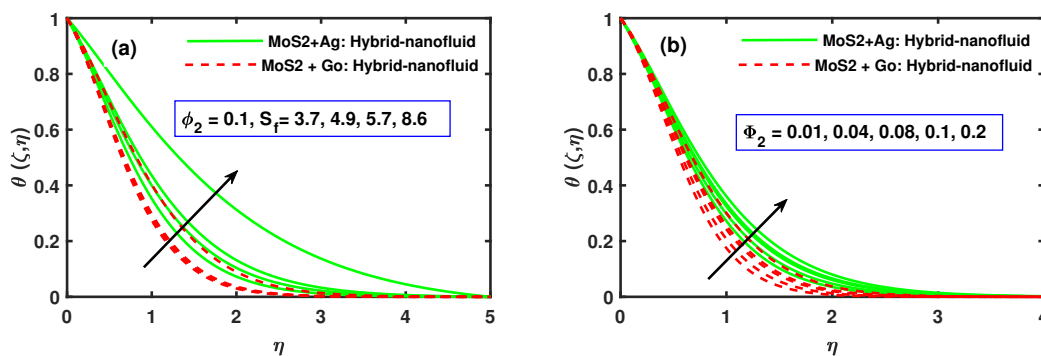

Figure 7. Fluctuation of $\theta(\zeta, \eta)$ along with S_f (shape factor parameter) and Φ_2 (nanoparticles volume fraction) at $\zeta = 1$.
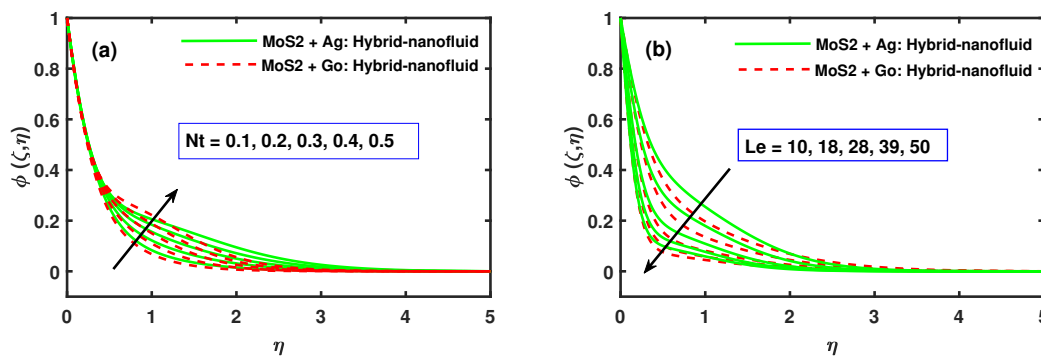

Figure 8. Fluctuation of $\phi(\zeta, \eta)$ along with Nt (thermophoresis) and Le (Lewis number) at $\zeta = 1$.
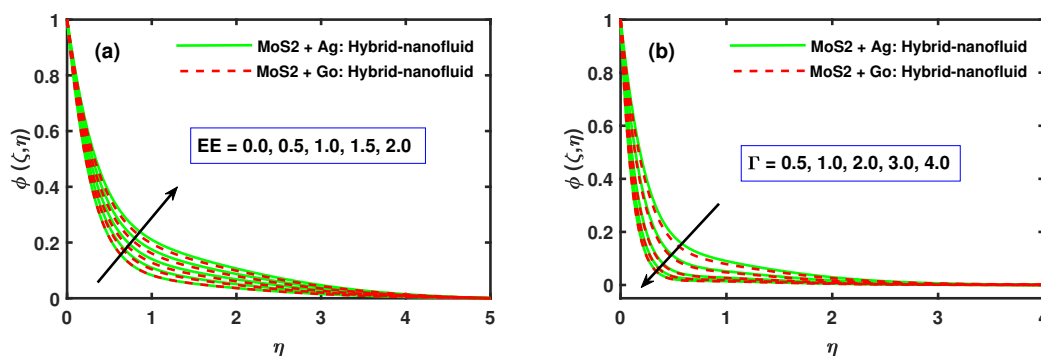

Figure 9. Fluctuation of $\phi(\zeta, \eta)$ along with EE (activation energy) and Γ (chemical reaction rate) at $\zeta = 1$.
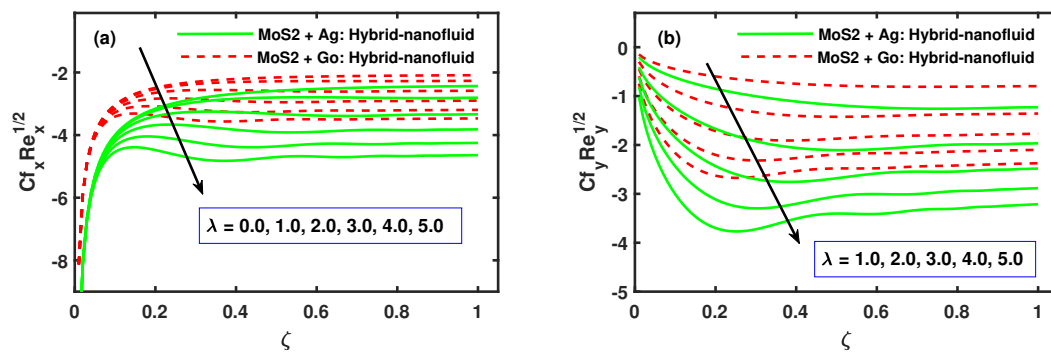
Figure 10. Fluctuation of $Cf_x Re_x^{1/2}$ and $Cf_y Re_y^{1/2}$ along with λ (rotating parameter).
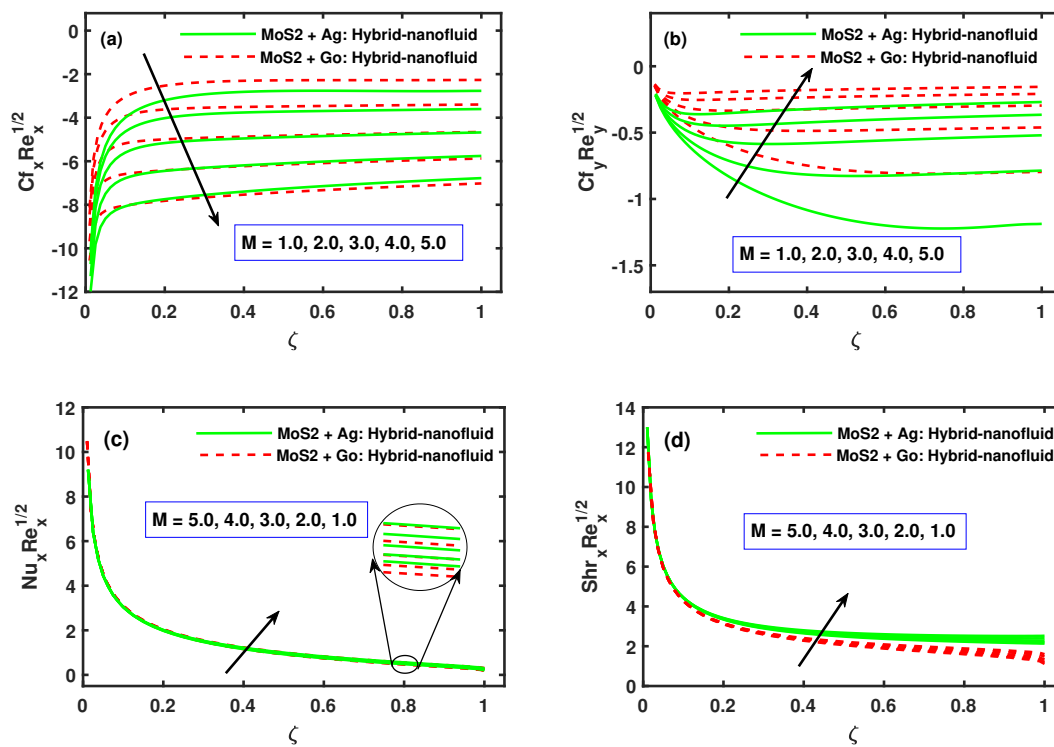

Figure 11. Fluctuation of $Cf_x Re_x^{1/2}$, $Cf_y Re_y^{1/2}$, $Nu_x Re_x^{1/2}$, and $Sh_x Re_x^{1/2}$ along with M (magnetic field).

The $Nu_x Re_x^{1/2}$ (reduced Nusselt number) and $Shr_x Re_x^{1/2}$ (reduced Sherwood number) are plotted respectively in Figure 11c,d against ζ and M. Both the quantities $Nu_x Re_x^{1/2}$ and $Shr_x Re_x^{1/2}$ are reduced sharply against the incremental values of M when $\zeta < 0.2$ then the decayed value become uniform for $\zeta > 0.2$. It is to be noted that $Nu_x Re_x^{1/2}$ is lesser in values for hybrid nano liquid than nano liquids but $Shr_x Re_x^{1/2}$ exhibit contrary trend. Figure 12a,b are drawn to indicate the variation in $Nu_x Re_x^{1/2}$ and $Shr_x Re_x^{1/2}$ when the parameters Nt, Nb and M are given variant inputs. The quantity $Nu_x Re_x^{1/2}$ undergoes a notable reduction with small increments in equal values of Nb and Nt but in contradiction $Shr_x Re_x^{1/2}$ attains higher values in this case. In Figure 13a,b sketches for $Nu_x Re_x^{1/2}$ and $Shr_x Re_x^{1/2}$ as delineated against Nt, Nb and λ exhibit the same trend as in Figure 12a,b.
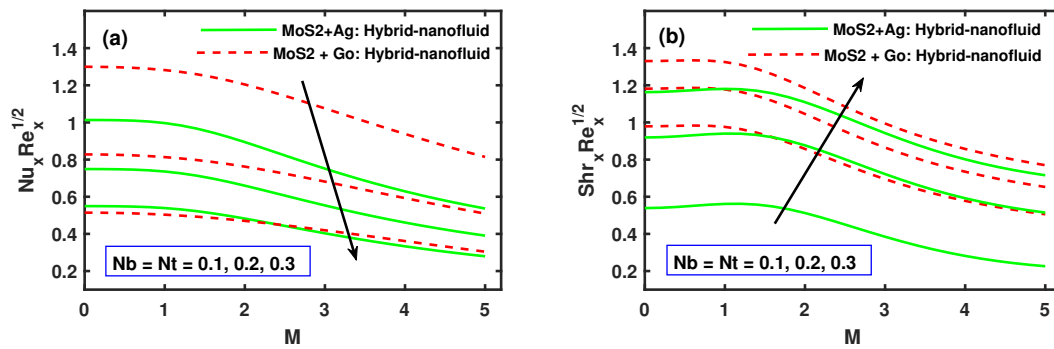
Figure 12. Fluctuation of $Nu_x Re_x^{1/2}$ and $Sh_x Re_x^{1/2}$ along with Nb, Nt (thermophoresis), and M (magnetic field).

Figure 14a,b shows the consolidated impact of the Nb (Brownian motion) and Nt (thermophoresis) on the reduced Nusselt number for two cases of Prandtl number, which is, $Pr = 2$ and $Pr = 10$, respectively. It is revealed that increments in thermophoresis and Brownian motion parameters recedes the wall heat transfer rate but Pr = 10.0 boost the wall heat transfer rate. At $Pr = 2.0$, Figure 14a demonstrate linear decay, however, monotonic decays are seen with higher value of $Pr = 10.0$ (see Figure 14b).
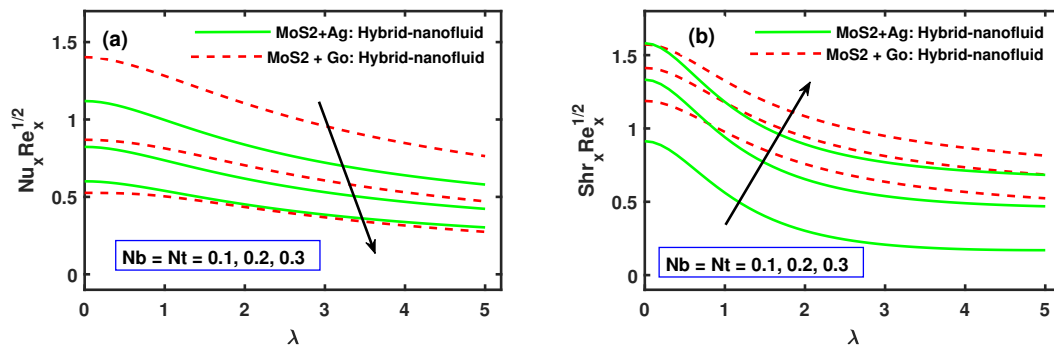

Figure 13. Fluctuation of $Nu_x Re_x^{1/2}$ and $Sh_x Re_x^{1/2}$ along with Nb, Nt (thermophoresis), and λ (rotating parameter).
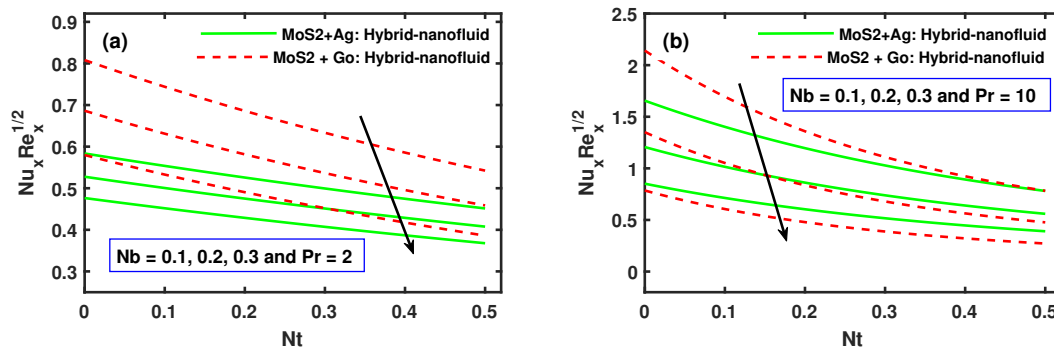

Figure 14. Fluctuation of $Nu_x Re_x^{1/2}$ along with Nb, Nt (thermophoresis), and Pr (Prandtl number) at $\zeta = 1$.

6. Conclusions

The finite element procedure is employed to examine the enhancement of thermal distribution for the magnetohydrodynamic rotational flow of hybrid nanofluids over a stretching plane. Numerical findings for velocity components, skin friction coefficients, temperature, Nusselt number, nano-particle volume fraction, and Sherwood number are computed for the hybrid phase and nanophase. Some of the major outcomes are reported below:

- The primary velocity component $f'(\zeta, \eta)$ decreases monotonically and the magnitude of secondary velocity component $g(\zeta, \eta)$ diminishes significantly when magnetic parameter M, rotational parameter λ and unsteadiness parameter τ are incremented.
- It is also observed that velocity $f'(\zeta, \eta)$ is slightly faster for hybrid phase Go-MoS$_2$ than hybrid phase Ag-MoS$_2$ but the velocity $g(\zeta, \eta)$ presents contrary behavior for the two nano phases.
- The incremental inputs of parameters M, Nt, λ, Nb, τ, and S_f have augmented the temperature of nanofluid.
- It is mentionable that temperature for hybrid nano liquids Ag-MoS$_2$ attains higher values than the hybrid fluid Go-MoS$_2$.
- The nanoparticle concentration $\phi(\zeta, \eta)$ is incremented with exceeding values of M, Nt, and Nb but it reduces against Lewis number Le. The nao particle concentration $\phi(\zeta, \eta)$ undergoes a fluctuating distribution with increment in τ.
- The concentration values for hybrid nano liquids Go-MoS$_2$ is lesser as compared with that of hybrid liquids Ag-MoS$_2$.
- The coefficients of skin friction ($Cf_x Re_x^{1/2}, Cf_y Re_y^{1/2}$) along x- and y-directions respectively are augmented notably for $\xi < 0.15$ and for $\xi > 0.15$ (nearly) these quantities become uniform for a given λ and M.
- The $Nu_x Re_x^{1/2}$ (reduced Nusselt number) and $Shr_x Re_x^{1/2}$ (reduced Sherwood number) are reduced sharply against the incremental values of M when $\zeta < 0.2$ then the decayed value become uniform for $\zeta > 0.2$.
- It is to be noted that $Nu_x Re_x^{1/2}$ and $Shr_x Re_x^{1/2}$ are lesser in values for hybrid nanofluids Ag-MoS$_2$ than hybrid liquids Go-MoS$_2$.

Through this computational effort, we have successfully elucidated the parametric impacts on the flow of two hybrid phases. The monotonic differences of the results for two-hybrid phases are clearly observed. This study may be extended for three or more hybrid phases to point out the most effectual among them.

Author Contributions: B.A. and R.A.N. modeled the problem and wrote the manuscript. D.H. complete the formal analysis and revision. O.M.A. and S.H. thoroughly checked the mathematical modeling, English corrections, formal analysis, and revision. B.A. solved the problem using MATLAB software. D.H. and R.A.N.: writing—review and editing. All authors finalized the manuscript after its internal evaluation. All authors have read and agreed to the published version of the manuscript.

Conflicts of Interest: The authors declare no conflict of interest.

Nomenclature

T	non-dimensional temperature, K	T_w	Temperature at surface, K
C	non-dimensional nanoparticles concentration	C_w	Concentration at surface
T_∞	temperature away from the surface, K	GO	Graphene oxide
C_∞	concentration away from the surface	Ω	angular velocity, s^{-1}
Cf_x	skin friction at x-direction	(u_1, u_2, u_3)	Velocity components
Cf_y	skin friction at y-direction	u_w	velocity of stretching sheet, ms^{-1}
Nu_x	Nusselt number	Sh_x	Sherwood number
ν_{nf}	Kinematic viscosity of nanofluid, $m^{-2}s^{-1}$	Nb	Brownian motion parameter
Nt	thermophoresis parameter	ρ_{nf}	Density of nanofluid, Kgm^{-3}
$\tilde{D}_T$	Thermophoretic diffusion coefficient	$\tilde{D}_B$	Brownian diffusion coefficient
Cp	specific heat at constant pressure, $JKg^{-1}K^{-1}$	B_0	Uniform magnetic field
σ_{nf}	Electrical conductivity of nanofluid, $Kg^{-1}m^3A^2$	p	pressure, $Kgm^{-1}s^{-1}$
Φ_1	first nanoparticle's volume fraction	MoS_2	Molybdenum disulfide
Φ_2	second nanoparticle's volume fraction	(x, y, z)	Cartesian co-ordinates
Φ	volume fraction	Ag	Silver
E	Activation energy	Pr	Prandtl number
s_f	empirical shape factor of nanoparticles	m	Fitted rate constant
μ_{nf}	dynamic viscosity of nanofluid, $Kgm^{-1}s^{-1}$	λ	rotation parameter
κ	thermal conductivity, $Wm^{-1}K^{-1}$	t	time, s^{-1}
q_w	surface heat flux, Wm^{-2}	Le	Lewis number
κ_{nf}	thermal conductivity of the nanofluid, $Wm^{-1}K^{-1}$	η	dimensionless variable
κ_f	thermal conductivity of the fluid, $Wm^{-1}K^{-1}$	M^2	magnetic parameter
nf	stands for nanofluid	hnf	stands for hybrid nanofluid
κ_{hnf}	thermal conductivity of hybrid nanofluid	κ_{bf}	thermal conductivity of base liquid

References

1. Maxwell, J. *Electricity and Magnetism, Clarendon*; Oxford Press: Oxford, UK, 1873.
2. Choi, S.U.; Eastman, J.A. *Enhancing Thermal Conductivity of Fluids with Nanoparticles*; Technical Report; Argonne National Lab.: Lemont, IL, USA, 1995.
3. Kang, H.U.; Kim, S.H.; Oh, J.M. Estimation of thermal conductivity of nanofluid using experimental effective particle volume. *Exp. Heat Transf.* **2006**, *19*, 181–191. [CrossRef]
4. Ghadikolaei, S.; Yassari, M.; Sadeghi, H.; Hosseinzadeh, K.; Ganji, D. Investigation on thermophysical properties of TiO_2-Cu/H_2O hybrid nanofluid transport dependent on shape factor in MHD stagnation point flow. *Powder Technol.* **2017**, *322*, 428–438. [CrossRef]
5. Zeeshan, A.; Shehzad, N.; Ellahi, R.; Alamri, S.Z. Convective Poiseuille flow of Al_2O_3-EG nanofluid in a porous wavy channel with thermal radiation. *Neural Comput. Appl.* **2018**, *30*, 3371–3382. [CrossRef]
6. Anwar, M.S.; Rasheed, A. Heat transfer at microscopic level in a MHD fractional inertial flow confined between non-isothermal boundaries. *Eur. Phys. J. Plus* **2017**, *132*, 305. [CrossRef]
7. Dinarvand, S.; Hosseini, R.; Pop, I. Homotopy analysis method for unsteady mixed convective stagnation-point flow of a nanofluid using Tiwari-Das nanofluid model. *Int. J. Numer. Methods Heat Fluid Flow* **2016**, *26*, 40–62. [CrossRef]
8. Mabood, F.; Ibrahim, S.; Kumar, P.; Khan, W. Viscous dissipation effects on unsteady mixed convective stagnation point flow using Tiwari-Das nanofluid model. *Results Phys.* **2017**, *7*, 280–287. [CrossRef]
9. Dinarvand, S.; Pop, I. Free-convective flow of copper/water nanofluid about a rotating down-pointing cone using Tiwari-Das nanofluid scheme. *Adv. Powder Technol.* **2017**, *28*, 900–909. [CrossRef]
10. Aghamajidi, M.; Yazdi, M.; Dinarvand, S.; Pop, I. Tiwari-Das nanofluid model for magnetohydrodynamics (MHD) natural-convective flow of a nanofluid adjacent to a spinning down-pointing vertical cone. *Propuls. Power Res.* **2018**, *7*, 78–90. [CrossRef]
11. Ghadikolaei, S.; Hosseinzadeh, K.; Ganji, D. Investigation on three dimensional squeezing flow of mixture base fluid (ethylene glycol-water) suspended by hybrid nanoparticle (Fe_3O_4-Ag) dependent on shape factor. *J. Mol. Liq.* **2018**, *262*, 376–388. [CrossRef]

12. Izadi, M.; Mehryan, S.; Sheremet, M.A. Natural convection of CuO-water micropolar nanofluids inside a porous enclosure using local thermal non-equilibrium condition. *J. Taiwan Inst. Chem. Eng.* **2018**, *88*, 89–103. [CrossRef]

13. Xu, H.; Xing, Z. The lattice Boltzmann modeling on the nanofluid natural convective transport in a cavity filled with a porous foam. *Int. Commun. Heat Mass Transf.* **2017**, *89*, 73–82. [CrossRef]

14. Ghadikolaei, S.; Hosseinzadeh, K.; Hatami, M.; Ganji, D. MHD boundary layer analysis for micropolar dusty fluid containing Hybrid nanoparticles (Cu-Al$_2$O$_3$) over a porous medium. *J. Mol. Liq.* **2018**, *268*, 813–823. [CrossRef]

15. Solomon, A.B.; Sharifpur, M.; Ottermann, T.; Grobler, C.; Joubert, M.; Meyer, J.P. Natural convection enhancement in a porous cavity with Al$_2$O$_3$-Ethylene glycol/water nanofluids. *Int. J. Heat Mass Transf.* **2017**, *108*, 1324–1334. [CrossRef]

16. Buongiorno, J. Convective transport in nanofluids. *J. Heat Transf.* **2006**, *28*, 240–250. [CrossRef]

17. Bhatti, M.M.; Rashidi, M.M. Effects of thermo-diffusion and thermal radiation on Williamson nanofluid over a porous shrinking/stretching sheet. *J. Mol. Liq.* **2016**, *221*, 567–573. [CrossRef]

18. Hayat, T.; Waqas, M.; Shehzad, S.; Alsaedi, A. A model of solar radiation and Joule heating in magnetohydrodynamic (MHD) convective flow of thixotropic nanofluid. *J. Mol. Liq.* **2016**, *215*, 704–710. [CrossRef]

19. Waqas, H.; Khan, S.U.; Imran, M.; Bhatti, M. Thermally developed Falkner–Skan bioconvection flow of a magnetized nanofluid in the presence of a motile gyrotactic microorganism: Buongiorno's nanofluid model. *Phys. Scr.* **2019**, *94*, 115304. [CrossRef]

20. Khan, W.A.; Uddin, M.J.; Ismail, A.M. Hydrodynamic and thermal slip effect on double-diffusive free convective boundary layer flow of a nanofluid past a flat vertical plate in the moving free stream. *PLoS ONE* **2013**, *8*, e54024. [CrossRef]

21. Nayak, M. MHD 3D flow and heat transfer analysis of nanofluid by shrinking surface inspired by thermal radiation and viscous dissipation. *Int. J. Mech. Sci.* **2017**, *124*, 185–193. [CrossRef]

22. Rasheed, A.; Anwar, M.S. Interplay of chemical reacting species in a fractional viscoelastic fluid flow. *J. Mol. Liq.* **2019**, *273*, 576–588. [CrossRef]

23. Naz, R.; Noor, M.; Hayat, T.; Javed, M.; Alsaedi, A. Dynamism of magnetohydrodynamic cross nanofluid with particulars of entropy generation and gyrotactic motile microorganisms. *Int. Commun. Heat Mass Transf.* **2020**, *110*, 104431. [CrossRef]

24. Hussain, S.; Ali, B.; Ahmad, F. MHD boundary layer flow and heat transfer for micropolar fluids over a shrinking sheet. *J. Appl. Environ. Biol. Sci* **2015**, *5*, 330–338.

25. Zohra, F.T.; Uddin, M.J.; Ismail, A.I. Magnetohydrodynamic bio-nanoconvective Naiver slip flow of micropolar fluid in a stretchable horizontal channel. *Heat Transfer—Asian Res.* **2019**, *48*, 3636–3656. [CrossRef]

26. Ali, B.; Ahmad, F.; Hussain, S.; Rasheed, U. MHD flow and heat transfer through porous medium over an exponentially shrinking permeable surface. *Sci. Int. (Lahore)* **2015**, *27*, 3961–3964.

27. Faraz, F.; Imran, S.M.; Ali, B.; Haider, S. Thermo-diffusion and multi-slip effect on an axisymmetric Casson flow over a unsteady radially stretching sheet in the presence of chemical reaction. *Processes* **2019**, *7*, 851. [CrossRef]

28. Aziz, A.; Muhammad, T.; Alsaedi, A.; Hayat, T. An optimal study for 3D rotating flow of Oldroyd-B nanofluid with convectively heated surface. *J. Braz. Soc. Mech. Sci. Eng.* **2019**, *41*, 236. [CrossRef]

29. Mustafa, M.; Ahmad, R.; Hayat, T.; Alsaedi, A. Rotating flow of viscoelastic fluid with nonlinear thermal radiation: a numerical study. *Neural Comput. Appl.* **2018**, *29*, 493–499. [CrossRef]

30. Wang, C. Stretching a surface in a rotating fluid. *Z. FÜR Angew. Math. Und Phys. Zamp* **1988**, *39*, 177–185. [CrossRef]

31. Takhar, H.S.; Chamkha, A.J.; Nath, G. Flow and heat transfer on a stretching surface in a rotating fluid with a magnetic field. *Int. J. Therm. Sci.* **2003**, *42*, 23–31. [CrossRef]

32. Nazar, R.; Amin, N.; Filip, D.; Pop, I. Unsteady boundary layer flow in the region of the stagnation point on a stretching sheet. *Int. J. Eng. Sci.* **2004**, *42*, 1241–1253. [CrossRef]

33. Khan, M.; Salahuddin, T.; Yousaf, M.M.; Khan, F.; Hussain, A. Variable diffusion and conductivity change in 3d rotating Williamson fluid flow along with magnetic field and activation energy. *Int. J. Numer. Methods Heat Fluid Flow* **2019**. [CrossRef]

34. Ibrahim, W. Three dimensional rotating flow of Powell-Eyring nanofluid with non-Fourier's heat flux and non-Fick's mass flux theory. *Results Phys.* **2018**, *8*, 569–577. [CrossRef]

35. Kumar, R.; Kumar, R.; Shehzad, S.A.; Sheikholeslami, M. Rotating frame analysis of radiating and reacting ferro-nanofluid considering Joule heating and viscous dissipation. *Int. J. Heat Mass Transf.* **2018**, *120*, 540–551. [CrossRef]

36. Jusoh, R.; Nazar, R.; Pop, I. Magnetohydrodynamic rotating flow and heat transfer of ferrofluid due to an exponentially permeable stretching/shrinking sheet. *J. Magn. Magn. Mater.* **2018**, *465*, 365–374. [CrossRef]

37. Jawad, M.; Shah, Z.; Islam, S.; Majdoubi, J.; Tlili, I.; Khan, W.; Khan, I. Impact of nonlinear thermal radiation and the viscous dissipation effect on the unsteady three-dimensional rotating flow of single-wall carbon nanotubes with aqueous suspensions. *Symmetry* **2019**, *11*, 207. [CrossRef]

38. Ali, B.; Yu, X.; Sadiq, M.T.; Rehman, A.U.; Ali, L. A Finite Element Simulation of the Active and Passive Controls of the MHD Effect on an Axisymmetric Nanofluid Flow with Thermo-Diffusion over a Radially Stretched Sheet. *Processes* **2020**, *8*, 207. [CrossRef]

39. Khan, S.A.; Nie, Y.; Ali, B. Multiple Slip Effects on Magnetohydrodynamic Axisymmetric Buoyant Nanofluid Flow above a Stretching Sheet with Radiation and Chemical Reaction. *Symmetry* **2019**, *11*, 1171. [CrossRef]

40. Rana, P.; Bhargava, R.; Bég, O.A. Finite element simulation of unsteady magneto-hydrodynamic transport phenomena on a stretching sheet in a rotating nanofluid. *Proc. Inst. Mech. Eng. Part J. Nanoeng. Nanosyst.* **2013**, *227*, 77–99. [CrossRef]

41. Abbas, Z.; Javed, T.; Sajid, M.; Ali, N. Unsteady MHD flow and heat transfer on a stretching sheet in a rotating fluid. *J. Taiwan Inst. Chem. Eng.* **2010**, *41*, 644–650. [CrossRef]

42. Bakar, N.A.A.; Bachok, N.; Arifin, N.M. Rotating flow over a stretching sheet in nanofluid using Buongiorno model and thermophysical properties of nanoliquids. In *AIP Conference Proceedings*; AIP Publishing LLC: Melville, NY, USA, 2017; Volume 1870, p. 040017.

43. Ramaiah K, D.; Kotha, G.; Thangavelu, K. MHD rotating flow of a Maxwell fluid with Arrhenius activation energy and non-Fourier heat flux model. *Heat Transf.* **2020**, *49*, 2209–2227. [CrossRef]

44. Ghadikolaei, S.; Gholinia, M. 3D mixed convection MHD flow of GO−MoS$_2$ hybrid nanoparticles in H$_2$O−−(CH$_2$OH)$_2$ hybrid base fluid under the effect of H$_2$ bond. *Int. Commun. Heat Mass Transf.* **2020**, *110*, 104371. [CrossRef]

45. Nazar, R.; Amin, N.; Pop, I. Unsteady boundary layer flow due to a stretching surface in a rotating fluid. *Mech. Res. Commun.* **2004**, *31*, 121–128. [CrossRef]

46. Shafique, Z.; Mustafa, M.; Mushtaq, A. Boundary layer flow of Maxwell fluid in rotating frame with binary chemical reaction and activation energy. *Results Phys.* **2016**, *6*, 627–633. [CrossRef]

47. Dinarvand, S.; Rostami, M.N. Three-dimensional squeezed flow of aqueous magnetite–graphene oxide hybrid nanofluid: A novel hybridity model with analysis of shape factor effects. *Proc. Inst. Mech. Eng. Part J. Process. Mech. Eng.* **2020**, *234*, 193–205. [CrossRef]

48. Hamid, M.; Usman, M.; Zubair, T.; Haq, R.U.; Wang, W. Shape effects of MoS$_2$ nanoparticles on rotating flow of nanofluid along a stretching surface with variable thermal conductivity: A Galerkin approach. *Int. J. Heat Mass Transf.* **2018**, *124*, 706–714. [CrossRef]

49. Rostami, M.N.; Dinarvand, S.; Pop, I. Dual solutions for mixed convective stagnation-point flow of an aqueous silica–alumina hybrid nanofluid. *Chin. J. Phys.* **2018**, *56*, 2465–2478. [CrossRef]

50. Rana, P.; Bhargava, R. Numerical study of heat transfer enhancement in mixed convection flow along a vertical plate with heat source/sink utilizing nanofluids. *Commun. Nonlinear Sci. Numer. Simul.* **2011**, *16*, 4318–4334. [CrossRef]

51. Ali, L.; Liu, X.; Ali, B.; Mujeed, S.; Abdal, S. Finite Element Analysis of Thermo-Diffusion and Multi-Slip Effects on MHD Unsteady Flow of Casson Nano-Fluid over a Shrinking/Stretching Sheet with Radiation and Heat Source. *Appl. Sci.* **2019**, *9*, 5217. [CrossRef]

52. Ali, B.; Nie, Y.; Khan, S.A.; Sadiq, M.T.; Tariq, M. Finite Element Simulation of Multiple Slip Effects on MHD Unsteady Maxwell Nanofluid Flow over a Permeable Stretching Sheet with Radiation and Thermo-Diffusion in the Presence of Chemical Reaction. *Processes* **2019**, *7*, 628. [CrossRef]

53. Uddin, M.; Rana, P.; Bég, O.A.; Ismail, A.M. Finite element simulation of magnetohydrodynamic convective nanofluid slip flow in porous media with nonlinear radiation. *Alex. Eng. J.* **2016**, *55*, 1305–1319. [CrossRef]

54. Ali, L.; Liu, X.; Ali, B.; Mujeed, S.; Abdal, S. Finite Element Simulation of Multi-Slip Effects on Unsteady MHD Bioconvective Micropolar nanofluid Flow Over a Sheet with Solutal and Thermal Convective Boundary Conditions. *Coatings* **2019**, *9*, 842. [CrossRef]

55. Reddy, J.N. *Solutions Manual for an Introduction to the Finite Element Method*; McGraw-Hill: New York, NY, USA, 1993; p. 41.

56. Jyothi, K.; Reddy, P.S.; Reddy, M.S. Carreau nanofluid heat and mass transfer flow through wedge with slip conditions and nonlinear thermal radiation. *J. Braz. Soc. Mech. Sci. Eng.* **2019**, *41*, 415. [CrossRef]

57. Reddy, G.J.; Raju, R.S.; Rao, J.A. Influence of viscous dissipation on unsteady MHD natural convective flow of Casson fluid over an oscillating vertical plate via FEM. *Ain Shams Eng. J.* **2018**, *9*, 1907–1915. [CrossRef]

58. Ali, B.; Naqvi, R.A.; Haider, A.; Hussain, D.; Hussain, S. Finite Element Study of MHD Impacts on the Rotating Flow of Casson Nanofluid with the Double Diffusion Cattaneo—Christov Heat Flux Model. *Mathematics* **2020**, *8*, 1555. [CrossRef]

59. Ali, B.; Rasool, G.; Hussain, S.; Baleanu, D.; Sehrish, B. Finite Element Study of Magnetohydrodynamics (MHD) and Activation Energy in Darcy–Forchheimer Rotating Flow of Casson Carreau Nanofluid. *Processes* **2020**, *8*, 1185. [CrossRef]

60. Butt, A.S.; Ali, A.; Mehmood, A. Study of flow and heat transfer on a stretching surface in a rotating Casson fluid. *Proc. Natl. Acad. Sci. India Sect. Phys. Sci.* **2015**, *85*, 421–426. [CrossRef]